

# Human Perception-Inspired Grain Segmentation Refinement Using Conditional Random Fields

Doruk Aksoy<sup>1,\*</sup>, Huolin L. Xin<sup>2</sup>, Timothy J. Rupert<sup>1,3</sup>, William J. Bowman<sup>1,\*</sup>

<sup>1</sup> Department of Materials Science and Engineering, University of California, Irvine, CA 92697, USA

<sup>2</sup> Department of Physics and Astronomy, University of California, Irvine, CA 92697, USA

<sup>3</sup> Department of Mechanical and Aerospace Engineering, University of California, Irvine, CA 92697, USA

\* Corresponding authors: [daksoy@uci.edu](mailto:daksoy@uci.edu), [will.bowman@uci.edu](mailto:will.bowman@uci.edu)

## ABSTRACT

Accurate segmentation of interconnected line networks, such as grain boundaries in polycrystalline material microstructures, poses a significant challenge due to the fragmented masks produced by conventional computer vision algorithms, including convolutional neural networks. These algorithms struggle with thin masks, often necessitating intricate post-processing for effective contour closure and continuity. Addressing this issue, this paper introduces a fast, high-fidelity post-processing technique, leveraging domain knowledge about grain boundary connectivity and employing conditional random fields and perceptual grouping rules. This approach significantly enhances segmentation mask accuracy, achieving a 79% segment identification accuracy in validation with a U-Net model on electron microscopy images of a polycrystalline oxide. Additionally, a novel grain alignment metric is introduced, showing a 51% improvement in grain alignment, providing a more detailed assessment of segmentation performance for complex microstructures. This method not only enables rapid and accurate segmentation but also facilitates an unprecedented level of data analysis, significantly improving the statistical representation of grain boundary networks, making it suitable for a range of disciplines where precise segmentation of interconnected line networks is essential.

## KEYWORDS

Grain Segmentation, Grain Boundary Networks, Computer Vision, Conditional Random Fields,  
Microstructure, Electron Microscopy

## 1. INTRODUCTION

Integrating computer vision with electron microscopy has significantly enhanced efficiency in materials science by speeding up traditionally laborious and time-consuming processes<sup>1</sup>. The advancement of (scanning) transmission electron microscopy ((S)TEM) is pivotal in examining grain boundary (GB) networks and other microstructural features in hard materials like metals and ceramics<sup>2</sup>. These techniques yield insights into structural characteristics such as (dis)order<sup>3</sup>, dislocations<sup>4</sup>, phase transformations and GB segregation<sup>5</sup>. GB networks, often statistically represented<sup>6</sup>, require extensive data for analysis. Revealing large-scale information like average grain sizes facilitates high-throughput experiments<sup>7</sup> aimed at elucidating local GB properties<sup>2</sup> and atomic (dis)order<sup>3</sup>. However, developing these techniques is challenging due to the complex nature of grain structures and their boundaries in ceramics, metals, and composites<sup>8,9</sup>, involving issues like managing overlapping grains<sup>10</sup> and deciphering defects of different dimensionality such as GBs, triple junctions, and nodes<sup>11</sup>. This complexity is accentuated when analyzing GB networks, influenced by factors like crystallographic orientations, interfacial segregation, and varied local atomic environments, affecting the mechanical, electrical, chemical, and magnetic behavior of materials<sup>12-22</sup>. GBs range from ordered high-symmetry structures to high-energy disordered configurations<sup>23</sup>, with networks exhibiting intricate relationships due to energetic competition between interfacial planes, atomic sites, and solute-solute interactions<sup>24-26</sup>. Moreover, local ordering and local hardening can be influenced by solute segregation to GBs<sup>11,27</sup>. Therefore, developing predictive techniques is challenging, considering the multifaceted role of GBs where local atomic environments, segregation behaviors, and solute interactions are closely connected.

This complexity often results in (S)TEM image contrasts, posing a unique challenge for conventional segmentation methods in identifying GBs.

Addressing this, semantic segmentation – a computer vision strategy categorizing each pixel into a class<sup>28</sup> – emerges as a promising approach for autonomous grain segmentation. Historically, two techniques have been prominent: traditional image processing and modern computer vision techniques. Traditional methods focus on low-level image details, using techniques like thresholding<sup>29</sup>, morphological processing<sup>30</sup>, edge detection with preset filters<sup>31</sup>, unsupervised machine learning clustering<sup>32</sup>, watershed transformation<sup>33</sup>, and region-growing<sup>34</sup>. Their effectiveness often depends on image quality, influenced by factors like resolution, color balance, brightness, and gradient similarity<sup>35</sup>. Conversely, modern computer vision approaches, particularly convolutional neural networks (CNNs), provide a more sophisticated, high-level grain representation<sup>36–39</sup>. Architectures like DeepLab<sup>40</sup>, Mask R-CNN<sup>41</sup>, and U-Net<sup>42</sup> are employed for their adaptability to different image resolutions and consistent segmentation capabilities.

However, CNNs' large perception fields limit their ability to produce accurate pixel-level labels<sup>28</sup>, which poses a problem in an interconnected grain network where the segmentation mask is a few pixels wide with a label assigned to each pixel (e.g., 1: GB, 0: grain interior). Metrics like intersection-over-union (IoU) and Dice similarity coefficient (DSC) are used to assess the alignment of predicted masks with ground truth. But, in thin masks, even minor 1-pixel deviations significantly affect accuracy<sup>43</sup>. Researchers have pursued post-processing methods to enhance segmentation accuracy. While some model-specific approaches, like Li et al.<sup>44</sup>, have achieved remarkable accuracy rates, many post-processing methods lack general applicability across different scenarios. Main challenges include connecting adjacent pixels and removing isolated

ones, relying on user-defined thresholds. These methods often miss crucial constraints related to GBs, essential for accurate segmentation of complex grain structures.

Here, this work aims to address the gap in semantic segmentation for (S)TEM images of polycrystalline materials by introducing a versatile post-processing method to refine interconnected GB network masks. This method, based on insights into GB connectivity<sup>45</sup> and the interconnected nature of GB networks<sup>46</sup>, is designed for broad applicability across different crystalline materials. At its core, it employs segmentation masks from computer vision models to generate conditional probability maps using conditional random fields (CRFs), bridging gaps left by CNNs. The required feature functions for CRFs are selected based on perceptual grouping rules<sup>47</sup>. Applicable to any crystalline material with discernible grain structure, this method can be used as a post-processing step for various grain segmentation masks from imaging systems and vision algorithms, enabling real-time segmentation refinement. It marks a significant advancement for materials scientists, allowing rapid and precise GB segmentation in complex microstructures with poorly resolved boundaries, and enabling previously inaccessible large-scale data analysis, greatly enhancing statistical representation of GB networks.

## **2. RESULTS**

### **A Hierarchical CRF Architecture**

When labeling sequence is critical, such as for interface pixels, CRFs emerge as a versatile tool. As a discriminative model, CRFs calculate the conditional probability of a pixel or segment having the same label given a sequence of observations<sup>48</sup>. CRFs require feature functions,

mathematical representations of feature relationships<sup>48</sup>. To incorporate domain knowledge accompanying the CRF method, the feature functions can be selected based on perceptual grouping principles. These principles, derived from Gestalt laws of perceptual organization, describe how humans intuitively perceive and interpret the visual world<sup>47</sup> and are relevant to grain segmentation refinement, as illustrated in Fig. 1. Key principles include:

- The Law of Proximity, indicating that elements close together are perceived as a group. In Fig. 1a, clustered dots exemplify this, aiding in identifying nearby pixels or segments as part of the same GB, especially areas of closely packed or intersecting boundaries.
- The Law of Similarity, where similar elements are seen as related. Fig. 1b shows this with dots of the same color and shape, grouping pixels or segments with similar characteristics for continuous GB identification.
- The Law of Closure, involving the mind's tendency to complete incomplete figures, as in Fig. 1c. This helps in filling gaps in GB networks that appear broken, addressing challenges posed by poorly resolved and complex structures in TEM images.
- The Law of Good Figure (or Prägnanz), where complex images are perceived in their simplest form, as seen in Fig. 1d. This aligns with GBs' tendency to minimize energy by adopting simpler shapes, reflecting the natural formation and evolution of GBs in materials.
- The Law of Continuity, favoring smooth patterns. Fig. 1e demonstrates elements aligned in a line or curve as a cohesive group, essential for maintaining continuous and smooth paths consistent with the physical properties of grain structures.

## Gestalt Principles of Perceptual Grouping

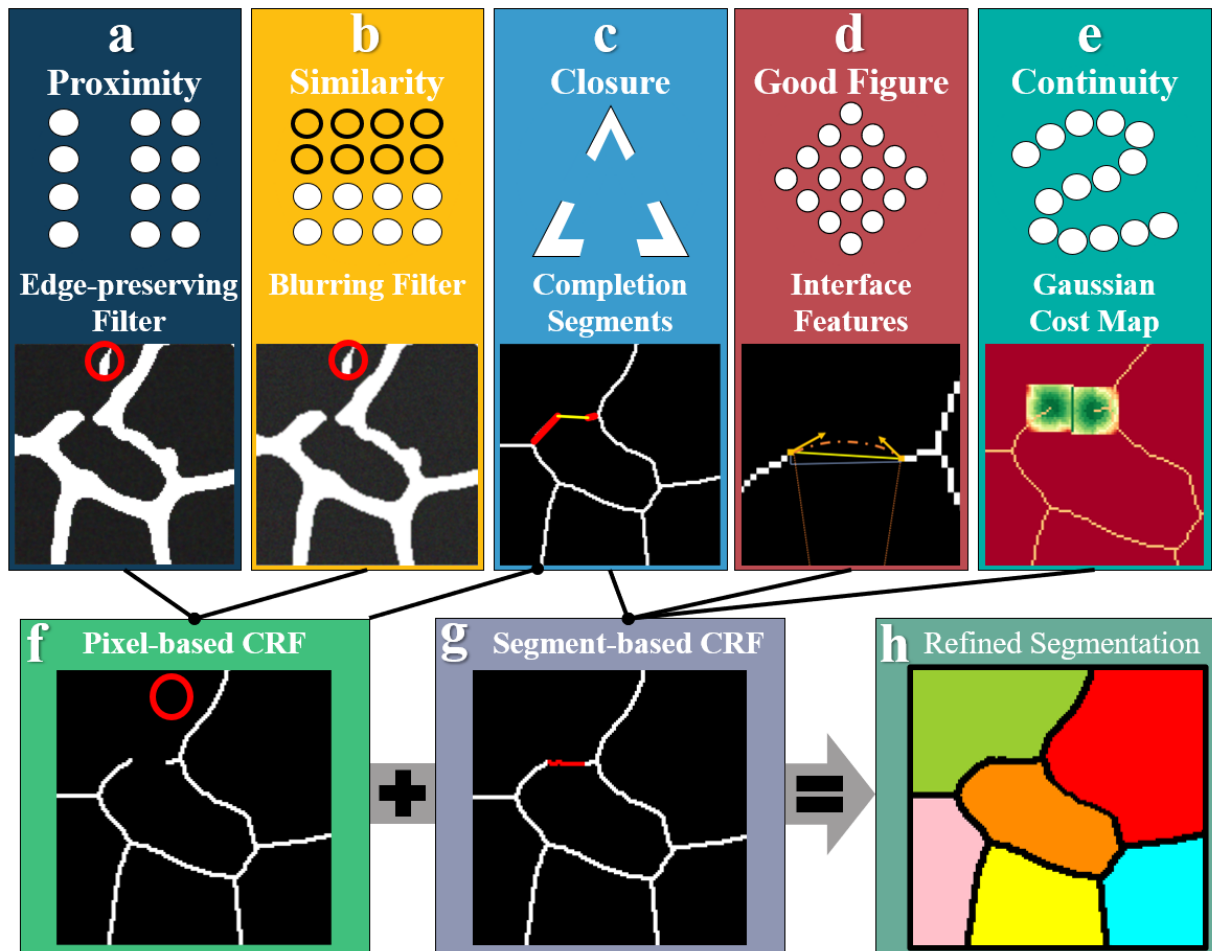


**Fig. 1. Overview of the utilization of the Gestalt principles of perceptual grouping.** a Proximity, b similarity, c closure, d good figure, and e continuity principles are satisfied through the use of f pixel-based CRF, and g segment-based CRFs resulting in h a refined segmentation. Each subplot provides a distinct visualization or method that contributes to the overarching theme of the paper, the robust analysis of GB networks.

Fully-connected independent pixelwise classification, often leading to patchy segmentation masks due to disregarding pixel relationships, is computationally demanding<sup>49</sup>. CRFs are preferred in such contexts as they effectively incorporate spatial relationships between pixels using pairwise costs. Early models primarily utilized grid graphs for defining these costs, which restricted information transfer among adjacent pixels<sup>50</sup>. However, the introduction of DenseCRF architectures allowed for fully connected graphs and more expressive pairwise potentials<sup>51,52</sup>. Higher-order CRFs for contour completion bring three key benefits to grain segmentation: (i) they foster label continuity among spatially and intensity-wise close pixels, (ii) facilitate modeling of long-range interactions, and (iii) use linear inequalities for modeling extension and continuity constraints.

In this work, a hierarchical methodology for object recognition and segmentation is introduced, combining pixel-based and segment-based definitions synergistically. The architecture is designed as a hypergraph, with vertices as individual pixels and hyperedges as segments. Inter-segment connections are construed as edges between hyperedges. Initially, a DenseCRF architecture<sup>51</sup> processes low-level pixel features (Figs. 1a, b, and f), which then inform the higher-level segment-based features, as illustrated in Figs. 1c-e, and g. This layered strategy allows for the integration of both local and global information, adhering to perceptual grouping principles.

The conditional probability of segments, which describes the probability distribution over all possible label configurations, is determined by minimizing Gibbs energy, comprising unary, pairwise, and higher-order terms. The unary potential encodes the likelihood of individual pixels belonging to specific segments, either complete or broken. This potential is derived from the pre-

trained CNNs that provide scores for each pixel, essentially constituting an initial coarse-grained classification. Local consistency is subsequently enforced through edge-preserving bilateral and Gaussian blur filters, yielding perceptually coherent regions by evaluating neighboring pixels' features like color and proximity, as shown in Figs. 1a and b. This effectively distinguishes segments in densely packed GBs, with non-conforming pixels eliminated, depicted in Figs. 1a, b, and f with red circles. Subsequently, a graph-based technique is employed to identify completion segments, which represent potential connections between broken segments. Due to computational limitations, only a subset of these completion segments, selected based on predetermined criteria, are deemed viable segments for further analysis. The various segment types are visually differentiated in Fig. 1c, with complete, broken, and completion segments shown in white, red, and yellow, respectively.

The pairwise potential, designed to capture long-range interactions, functions effectively on identified segments to maintain global consistency. It enforces completion and extension constraints, as described in a previous contour completion model<sup>53</sup>, aligning with the principle of closure illustrated in Fig. 1c. The completion constraint activates a completion segment only when its adjacent broken segment is active. Simultaneously, the extension constraint ensures that an active broken segment has at least one neighboring active completion segment, preserving the continuity and integrity of the GB structure.

A higher-order potential incorporates specific visual characteristics like contour sharpness, smoother segment transitions, angular differences between segments, and segment lengths. The model's complexity is managed by considering additional features such as the total effective length of connected segments and the angular deviation from ideal connection angles. This optimizes

simpler, more stable GB forms, adhering to the law of good figure, reflecting the natural evolution of GBs to minimize energy and simplify complex structures for perceptual coherence, as shown in Fig. 1d. Further details on the hierarchical CRF architecture are available in the Methods section.

In this composite architecture, the hypergraph method efficiently captures intricate relationships between pixels and segments, enabling a thorough representation of spatial and geometric features in the image. The primary goal is to achieve a binary label configuration that maximizes the conditional probability, representing the CRF's maximum *a posteriori* probability estimate. This poses a combinatorial optimization challenge, where the ideal solution is the label configuration maximizing this probability. This optimization problem can be posed as a mixed-integer linear programming (MILP) problem, which can then be solved to obtain the optimal label configuration.

Identifying the optimal label configuration involves determining local weights for interface features and global weights for unary, pairwise, and higher-order potentials. The optimal configuration is that which most closely approximates the ground truth, leading to an NP-hard combinatorial optimization problem. Being NP-hard, it is defined by the property that while the validity of a solution, like a label configuration, can be efficiently verified via the MILP equation, there is no polynomial-time algorithm for optimal resolution. Consequently, exact solutions to such NP-hard problems are computationally infeasible<sup>54</sup>, especially in images with hundreds of broken and completion segments, typical of fragmented GB networks.

To address this challenge, this study employs differential evolution to minimize the objective function, achieving a near-optimal solution. As an evolutionary algorithm and global optimization method, differential evolution iteratively refines candidate solutions, adjusting their weights based

on performance metrics within set bounds<sup>55</sup>. This process derives weights for the optimal label configuration by repeatedly solving the MILP with varied weight combinations. The resulting optimal label configuration, indicated by activated segments (marked as 1 by the CRF), facilitates the smooth connection of completion segments. This approach aligns with the law of continuity, essential for ensuring continuous, logically flowing GBs in the segmentation process, consistent with the physical nature of grain structures, as depicted in Fig. 1e.

Existing methods like the stochastic completion fields method<sup>56,57</sup> can trace smooth paths between points, yet they lack guaranteed solutions and can be computationally intensive. Hence, in this work, where the identification of GBs for subsequent chemical analysis is time-sensitive, a cost-based pathfinding algorithm is utilized to find the lowest-cost shortest path between the endpoints of a completion segment, denoted as the source and the sink. Cost maps are generated using isolated points and curving angles of each segment in the ideal label configuration, as shown in Fig. 2a. Costs are derived from probability distributions based on the natural curving angles of adjacent broken segments (Fig. 2b), aiding in connectivity assumptions at interfaces. This method mirrors GBs' energy-minimization tendency, favoring shorter, less costly paths similar to how GBs naturally form by reducing their area (length in a projection) to lower their energy state. The selected pathfinding algorithm is the A\* algorithm, a graph traversal and path search algorithm<sup>58</sup> that employs a heuristic function, here chosen to be the Chebyshev distance with 8-way directionality, with the rationale for this selection being elaborated in Supplementary Note 1. This algorithm starts from the source, moving towards the sink while tracking path and associated cost. Paths are reconstructed by backtracking the lowest-cost shortest paths identified by A\*, as in Fig. 2c. These paths, shown in Fig. 1g, connect broken segments in fragmented masks, resulting in

refined segmentation depicted in Fig. 1h, reflecting GBs' natural energy-minimizing behavior. Further details on the pathfinding algorithm can be found in Supplementary Note 1.

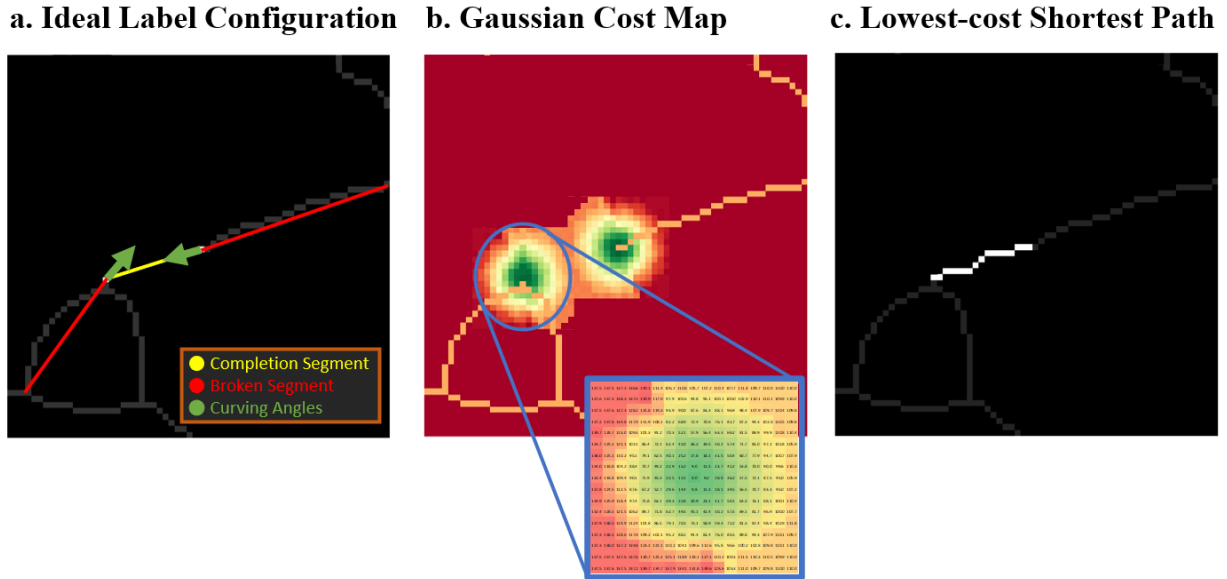


**Fig. 2. A cost-based pathfinding algorithm.** **a** The ideal label configuration with identified broken and completion segments, alongside curving angles. **b** The Gaussian cost map with varying color intensities and specific cost values. The inset illustrates the different costs assigned to pixels drawn from a 2D exact Gaussian distribution, based on the curving angle. **c** The lowest-cost shortest path is determined post-application of the A\* pathfinding algorithm.

## Implementation

To demonstrate this methodology, fragmented segmentation masks are generated from a trained computer vision algorithm on 20 manually annotated images of an electrically conducting polycrystalline oxide, acquired via STEM. This manual annotation, widely used in materials

science, involves tracing GBs to assess grain sizes and network structures for subsequent material property analysis. The annotated images serve as ground truth for model training, labeled as computer vision ground truth (CVGT) to differentiate from fragmented segmentation ground truth (FSGT). CVGT assesses the computer vision model's performance, while FSGT evaluates segmentation refinement. To enhance the robustness and generalizability of the model, data augmentation methods were carefully selected. Brightness adjustment is used to simulate variations in illumination, Gaussian blur to mimic slight focus variations common in microscopy, and rotation to ensure the model's insensitivity to orientation changes. These augmentations aim to produce a more versatile and adaptable computer vision algorithm. A modified U-Net architecture<sup>42</sup> with VGG16<sup>59</sup> as the encoder backbone is used for image segmentation. The model, focusing on segmentation accuracy over hyperparameter optimization, achieves a DSC of 0.72 in validation, aligning with benchmarks<sup>60</sup> and efficiently processes high-resolution images for detailed material structure analysis. For more information on the computer vision model, refer to the Methods section.

On the fragmented segmentation masks, pixel-based CRFs are applied, followed by the creation of the FSGT. FSGT is formed by manually labeling each identified completion and broken segment, following specific principles including consistent judgement across all images, marking the connection segments only if the natural curvatures of the broken segments appear to intersect and ensure non-occluding connections. These FSGTs aid in learning optimal weights and evaluating the proposed method's performance. In a sample image, Fig. 3a displays all segments identified by the algorithm, Fig. 3b the manually labeled FSGT, and Fig. 3c the best solution from the differential evolution algorithm, which corresponds to the minimum difference

in labeling configurations between the FSGT and MILP solution. Insets in Fig. 3 magnify portions where the CRF accurately predicts most segments. Fig. 3c illustrates newly identified grains from connected segments, enhancing segmentation accuracy, as the subsequent watershed algorithm identifies grains by continuous lines forming the boundary of closed geometric shapes.

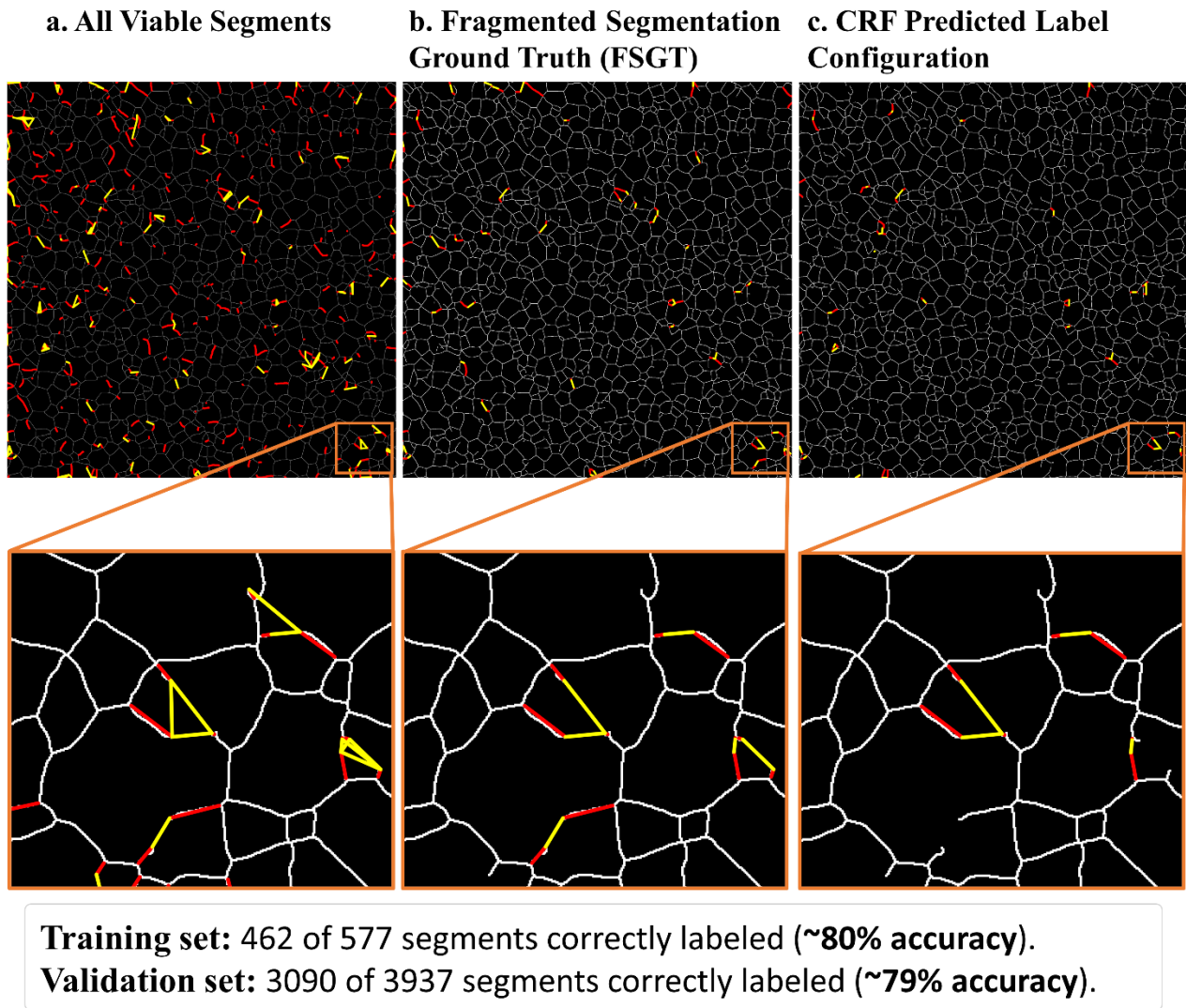


**Fig. 3. Detailed examination of the segment-based CRF labeling.** a All viable segments

identified by the algorithm. **b** The manually labeled fragmented segmentation ground truth (FSGT) with broken (red) and completion (yellow) segments. **c** The CRF predicted label configuration, illustrating the optimal segment connections post-differential evolution algorithm. Insets in each subplot offer a magnified view of selected areas, elucidating the finer details of segmentation.

### **Watershed Segmentation**

A marker-based watershed segmentation technique, based on geographical watershed principles<sup>33</sup>, is employed for image segmentation. This method converts the image into a topographical map with pixel values representing altitudes, applying the watershed transform to create catchment basins associated with distinct markers<sup>61</sup>. The basin boundaries, as shown in Fig. 4a, segment the image into distinct regions or grains. However, broken lines in the mask, such as those visible in Fig. 4a, can result in suboptimal segmentation. The grains in these plots appear as randomly colored shapes, except for the region depicted in the insets, where grain colors are matched manually for better visualization. More details about this method can be found in Supplementary Note 2. This segmentation is applied to three image types: (1) the original segmentation mask before post-processing (Fig. 4a), (2) the FSGT (Fig. 4b), and (3) the CRF solution (Fig. 4c). The figure shows that broken segments without viable completion segments are removed, and sections are smoothly connected, thereby enhancing segmentation. Insets in Fig. 4 demonstrate how the connections shown in Fig. 3c results in better grain segmentation, impacting the statistical representation of GB networks through improvements in grain shape and area. These segmented images are then used to evaluate the performance of the post-processing procedure.

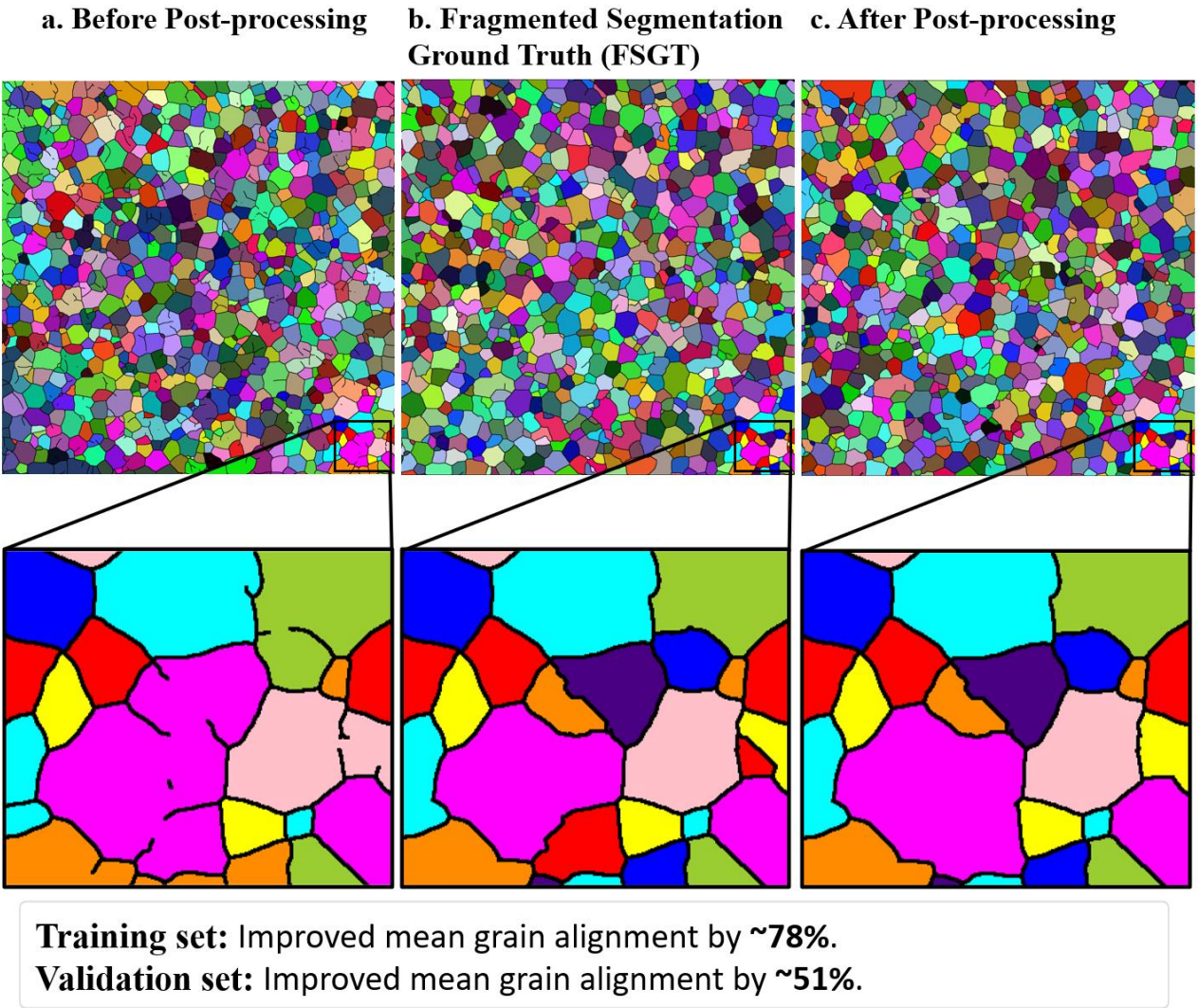


**Fig. 4. Image segmentation using marker-based watershed technique.** **a** Original segmentation mask before post-processing with visible broken segments. **b** Fragmented segmentation ground truth (FSGT) image that highlights the connections between the disconnected segments. **c** CRF solution corresponding to the optimal label configuration after post-processing, showing removal of dangling broken segments and smoother connections between sections. The

grains are randomly colored, except for the insets. Insets in each subplot provide a magnified view, emphasizing the differences in grain identification and segmentation performance.

### Performance Evaluation

In the segmentation performance evaluation, the post-processing procedure consistently improved various metrics, as shown in Table 1. Pixel accuracy, measuring correctly classified pixels against the total number, increased by 0.18% in the validation set from an already high baseline of 0.997 to 0.999, indicating near-perfect classification accuracy. To better assess segmentation masks, metrics such as IoU and DSC are often employed<sup>43</sup>. IoU measures the overlap of two masks by dividing their intersection by their union, while DSC puts greater emphasis on the overlapping region. IoU and DSC metrics exhibited an increase of 9.15% and 5.19% in the validation set due to post-processing, respectively. These improvements bring the final IoU and DSC values to 92.5% and 96.1% representing significant enhancements in segmentation accuracy, particularly for tasks involving complex grain structures. Calculation details for these metrics are provided in Supplementary Note 3. Additionally, grain-specific metrics, like the number of grains,  $N_G$ , and average grain size,  $V_G$ , also demonstrated notable improvements, detailed in Table 2. These enhancements were calculated as percentage improvements over the FSGT baseline, based on their relative differences.

<b>Table 1.</b> Comparison of segmentation performance evaluation metrics for both training and validation sets, highlighting the improvements achieved through post-processing.						
Metric	Training Set			Validation Set		
	FSGT /Before*	FSGT /After*	Percent Change	FSGT Before*	FSGT /After*	Percent Change
Pixel Accuracy	0.997	0.999	0.18%	0.997	0.999	0.18%
IoU	83.4%	92.5%	9.15%	83.4%	92.5%	9.15%
DSC	91.0%	96.1%	5.19%	91.0%	96.1%	5.19%

Accuracy	0.998	0.999	<b>0.18%</b>	0.997	0.999	<b>0.18%</b>
IoU	0.911	0.979	<b>6.78%</b>	0.833	0.925	<b>9.15%</b>
DSC	0.954	0.989	<b>3.58%</b>	0.909	0.961	<b>5.19%</b>
Precision	0.929	0.996	<b>6.66%</b>	0.853	0.967	<b>11.36%</b>
Recall	0.979	0.983	<b>0.39%</b>	0.973	0.955	<b>-1.77%</b>
Grain Alignment	777.8	174.2	<b>77.6%</b>	4062.7	2007.7	<b>50.6%</b>
* Metrics calculated by comparing the FSGT and the segmentation mask before or after post processing. The bold values indicate the percent changes in the metrics.						

**Table 2.** Metrics specific to grain attributes for both training and validation sets, illustrating the number of grains,  $N_G$  and average size of identified grains,  $V_G$  and their respective percent changes after post-processing.

Metric	Training Set				Validation Set			
	FSGT*	Before*	After*	Percent Change	FSGT*	Before*	After*	Percent Change
$N_G$	904	797	893	<b>10.62%</b>	1518	1206	1520	<b>20.69%</b>
$V_G$	4309.0	4812.8	4429.2	<b>8.90%</b>	10864.0	13293.4	11180.7	<b>19.45%</b>
* Metrics calculated for different segmentation masks, including the FSGT and the segmentation mask before and after post processing. The bold values indicate the percent changes in the metrics.								

An analysis of confusion matrices is presented in Fig. 5a for the training set and Fig. 5b for the validation set. In the training dataset, the CRF correctly predicts 462 out of 577 segments, achieving approximately 80% accuracy. For the validation set, it accurately predicts 3090 out of 3937 segments, a 79% success rate. Regarding time efficiency, manual labeling of the FSGT took roughly 41 minutes per 1000 segments, whereas the CRF labeled 1000 segments in about 15 milliseconds using an AMD Ryzen 9 5900X 12-Core Processor, markedly faster by five orders of magnitude. Additionally, weight learning, needed once per application, completes in around 47 minutes. For fully automated STEM imaging and spectroscopic data acquisition in GB network

chemical analysis, the CRF's rapid processing rate would enable time-efficient implementation needed to mitigate the effects of microscope instability such as specimen drift and lens defocus.

A novel metric for grain alignment is developed to overcome the limitations of traditional metrics in this specific segmentation context. This metric computes the average absolute difference between the areas of closely aligned regions in two labeled images, identified based on the proximity of their centroids. A smaller value for grain alignment indicates a higher degree of similarity in terms of grain size between the two images, making it an effective measure for comparing segmented regions, especially in the context of thin segmentation masks. Significant improvements in mean grain alignment, up to 78% in training and 51% in validation sets, are observed post-segmentation. These enhancements are critical as they significantly enhance the accuracy of statistical representation of grain size and location, leading to more precise analysis of GB networks, especially in densely packed or intersecting boundary regions.

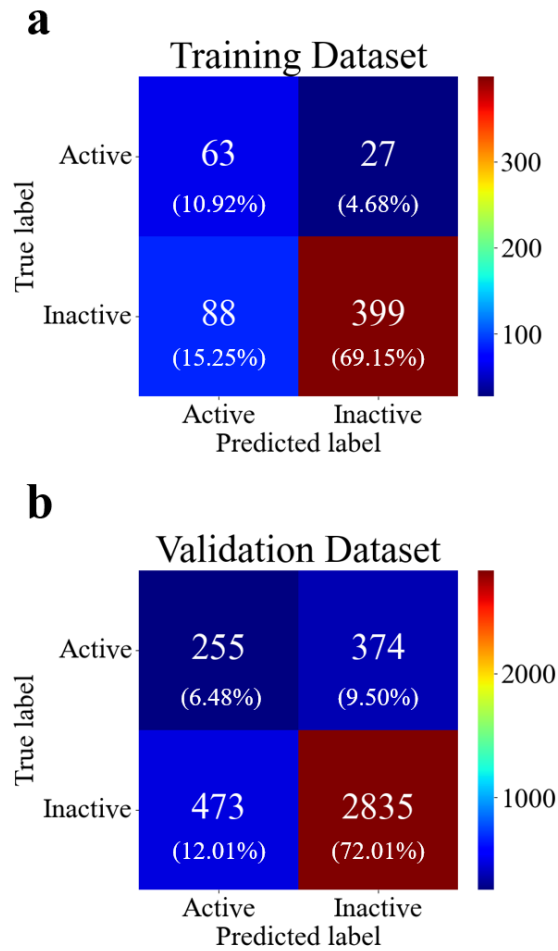


**Fig. 5. Detailed evaluation metrics for segmentation performance.** Confusion matrices illustrating the alignment of predicted segment labels with true labels for **a** the training set, and **b** the validation set. 'active' and 'inactive' denote segments identified as kept or discarded, respectively, highlighting the model's classification efficacy.

### 3. DISCUSSION

#### Beyond Conventional Metrics

Pixel accuracy focuses on the count of foreground and background pixels and neglects their spatial distribution, which limits its utility in single-pixel wide masks. In cases where discarded broken segment pixels equal the number of added completion segment pixels, pixel accuracy remains unchanged, potentially misrepresenting changes in spatial distribution. While high pixel accuracy may suggest superior performance, it can obscure spatial distribution nuances. IoU and DSC, although more nuanced, are sensitive to minor spatial variations, which is a notable limitation in thin masks. Nevertheless, improvements in these metrics post-processing affirm their utility in assessing the alignment of segmentation masks with ground truth.

Table 2 shows post-processing enhancements in actual segmented grains. Both the number of identified grains and average grain size align more closely with the ground truth post-processing, signifying not only improved alignment but also enhanced grain segmentation attributes. These advancements indicate a more accurate representation of grain size distribution and density, crucial for assessing mechanical and physical material properties. GBs considerably affect aspects like crack propagation, corrosion resistance, and mechanical strength, highlighting the importance of these improvements.

Table 1 and the confusion matrices in Fig. 5a and b reveal a decrease in recall for the validation set, suggesting the model's reduced sensitivity in identifying active segments post-processing. This could stem from unseen data or minor overfitting during training. These metrics primarily assess the model's proficiency in correctly labeling pixels or segments as active or inactive. However, in grain segmentation tasks that emphasize not only accurate pixel classification but also the morphological characteristics of the grains, such metrics may not fully capture the performance.

Addressing limitations in conventional metrics, a new metric, grain alignment, is proposed for evaluating segmentation performance. This metric involves identifying centroids of corresponding regions in two labeled images. For each grain in the first image, the closest centroid grain in the second image is determined, ensuring spatial proximity-based comparison. The absolute differences in the areas of these closely aligned regions are calculated and averaged to gauge size similarity, offering a robust measure for segmented region accuracy, particularly in thin masks. While this approach provides a robust metric, it's important to note the mean grain alignment metric difference between the training and validation dataset can be attributed to a few considerations. This discrepancy arises because accurately identifying grains requires all constituting lines to be connected. In fragmented images, unconnected lines can lead to incorrect grain identification, merging multiple grains into a single large one, and thus affecting the grain count and spatial distribution. Additionally, the post-processing's single-pass might leave some segments incomplete. This difference is more indicative of the validation set's complexities rather than a general limitation of the method. By identifying closely situated grains as part of the same boundary network, this method precisely represents microstructures, essential for accurate material behavior prediction, demonstrating its utility despite the noted dataset-specific challenges.

In addition to the demonstrated accuracy, the CRF's remarkable time efficiency is particularly valuable in materials science applications requiring real-time analysis. This rapid segmentation capability, in stark contrast to the time-consuming manual labeling process, allows for immediate GB identification post-image acquisition. Crucial in countering issues like drift in TEM imaging, real-time processing ensures analyses are based on accurately segmented, current images. This not only boosts analysis reliability but also enables dynamic, in-situ experimentation and

observation in materials science, where monitoring changes over time and under varying conditions is essential.

### **Comparing Standard and Specialized Ground Truths**

The CVGT and FSGT evaluate distinct aspects of segmentation, targeting specific criteria. The CVGT focuses on essential features for initial computer vision training, whereas the FSGT addresses specialized grain segmentation requirements, including unique post-processing needs such as continuous grain lines. Consequently, comparing post-processed results directly with the CVGT is inherently flawed. The CVGT, serving as a baseline for assessing computer vision algorithm performance, varies across images and is contingent on the computer vision output's quality. Therefore, it becomes an unstable and unreliable baseline for evaluating the post-processing procedure's performance, which inherently refines and alters the computer vision algorithm's initial segmentation.

Post-processing impacts metrics like IoU and DSC, influenced by the initial model's alignment with the CVGT. Generally, good alignment enhances these metrics post-processing, whereas poor alignment diminishes them. For instance, in Table 1, using the CVGT as ground truth, IoU and DSC in the training set decrease by 0.12% and 0.21%, respectively, despite a 78% improvement in grain alignment. This indicates that post-processing accentuates the initial segmentation's adherence to the CVGT. Therefore, to isolate the specific influence of the post-processing procedure, a comparison with the FSGT is essential. Additionally, the subjectivity in annotating GBs complicates evaluations. Consistency in CVGT and FSGT annotations is difficult due to specific grain characteristics, introducing variability in ground truths and affecting metrics. This

underlines the limitations of relying solely on CVGT for evaluation and the importance of including the FSGT for comprehensive assessment.

### **Towards Advanced Segmentation and Cross-Domain Applications**

Factors like hyperparameter optimization, model choice, and more training data can enhance baseline segmentation accuracy. Post-processing adjustments involve hyperparameters like maximum segment distance for selecting viable segments, field size, and pathfinding costs. Iteratively optimizing these hyperparameters is recommended for improved robustness and accuracy. This work also paves the way for joint CRF and CNN training. End-to-end trainable models, such as those that model CRFs and their feature functions as recurrent neural networks, can be appended to CNNs for training<sup>62</sup>, which are expected to yield even higher segmentation accuracies<sup>49</sup>.

In this study, T-junctions—connections between isolated points and segments—are not included, despite constituting about half of the training set's segment candidates. Their inclusion is expected to improve segmentation performance<sup>53</sup>, offering a fuller network representation. Beyond the seven interface features examined in this study, future iterations could integrate additional grain-related features, such as the Mullins grain growth model<sup>63</sup> to inform the algorithm about potential GB movements for enhanced predictive accuracy. Combining electron diffraction with optical reflectance measurements to estimate GB character<sup>64</sup>, and incorporating crystallographic orientation data, can provide detailed grain physical properties, aiding in segmentation refinement. Electron diffraction and optical reflectance could enhance GB identification, while crystallographic orientation might help differentiate grain types or phases.

Further segmentation enhancement might come from local neighborhood analysis using image features like brightness, color, texture<sup>65</sup>, and the intensity gradient along completion segments<sup>66</sup>. When the original image is accessible, contrast differences between grains and texture analyses could be employed between the original and the predicted masks<sup>67</sup>. This can link GB microstructure with material properties, aiding in predicting mechanical, thermal, and electrical behaviors<sup>68</sup>.

Implementing this post-processing procedure facilitates high-throughput experimental pipelines with reduced human supervision requirements, while maintaining comparable accuracies. S(TEM) images can be subjected to computer vision algorithms and subsequently analyzed using complementary methods such as electron diffraction and spectroscopies in a continuous pipeline. Fractional probabilities obtained from computer vision outputs can serve as unary terms in pixel-based CRFs, enhancing predictions and enabling confidence level assignments to each segment for targeted experiments<sup>69</sup>.

Statistical distribution information, such as average grain size, could be obtained and leveraged to improve segmentation performance. Outlying grains, indicative of abnormal growth, could be flagged for operator review. The post-processing procedure makes such data available to the operator, alongside candidate segments and their associated costs, thus facilitating a human-in-the-loop approach while expediting the process without compromising fidelity. The segment-based CRF approach exhibits strength in detecting closed contours in noisy environments<sup>53</sup>, a capability that can be harnessed to identify interfaces even in the presence of other image features like nano-precipitates or atomic details from S(TEM) without an additional classifier<sup>44</sup>.

Moreover, the utility of thin segmentation masks extends beyond the domain of materials science, finding applications in biomedical imaging for narrow or elongated structures. Areas of application include retinal blood vessel segmentation<sup>70</sup>, neuronal structure analysis<sup>71</sup>, coronary artery delineation in cardiac MRI<sup>72</sup>, tendon segmentation in musculoskeletal imaging<sup>73</sup>, lymphatic system studies<sup>74</sup>, and angiography for small blood vessels<sup>75</sup>. The methodology introduced in this work offers a new perspective and serves as a resource for other researchers, setting the stage for further advancements in segmentation mask optimization for interconnected line networks.

## **4. METHODS**

### **Image Acquisition and Annotation**

The 20 images that form the input dataset were high-angle annular dark field and annular bright field STEM images recorded with a Nion UltraSTEM100 aberration-corrected STEM operating at 60 kV. The material is an electrically conducting polycrystalline oxide, fluorite  $\text{Pr}_{0.1}\text{Ce}_{0.9}\text{O}_2$ , synthesized by pulsed laser deposition as a layer of nearly uniform thickness (~30 nm) atop an amorphous silicon nitride free standing substrate.

These images are digitized manually with a digital drawing tablet. GBs marked on the images constitute the CVGT, serving as targets for model training. Annotating both annular dark field and bright field images of the same areas at different times aims to minimize human operator bias. Regions marked as interfaces in both image types reinforce the trained model's predictions of interface pixels.

## **Pre-processing**

The acquired images and masks undergo pre-processing for data augmentation, manipulation, and dataset partitioning for the computer vision algorithm. An augmentation pipeline, including brightness adjustments (factors between 0.8 and 1.2), Gaussian blur (sigma values of 0.5 to 1.5), and rotation (between  $-45^\circ$  to  $45^\circ$ ), simulates real experimental conditions. Each image receives 20 augmentations by randomly applying these adjustments, resulting in 400 augmented images. A sample of these augmentations is displayed in Fig. 6a. The dataset is systematically divided into training, validation, and test subsets with split ratios of 70%, 20%, and 10%, ensuring balanced data distribution across all subsets.

## **Computer Vision Model**

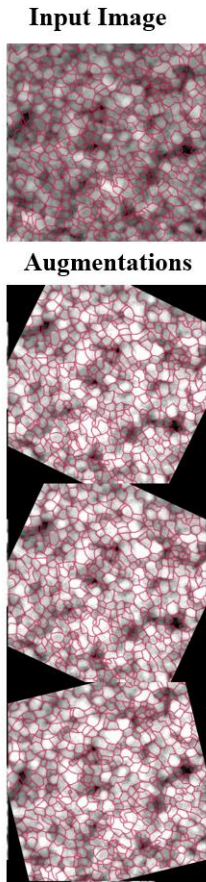
A computer vision algorithm for image segmentation is developed using a modified U-Net architecture<sup>42</sup>, with VGG16 model<sup>59</sup> serving as the encoder backbone. This architecture, effective for varying image resolutions, features a symmetric encoder-decoder structure<sup>42</sup> with skip connections to preserve key details lost during downscaling<sup>76</sup>. It consists of a contracting path capturing low-level features while reducing spatial size and increasing channels, and an expanding path that upscales these features to original size, reducing channels and capturing high-level features for accurate segmentation<sup>42</sup>. The model includes four decoder blocks, each with a 2D convolution layer matching the corresponding encoder layer's channels, followed by concatenation with the encoder's skip connection and two convolutional blocks with batch normalization and ReLU activation. The final output uses a sigmoid function. Compiled with Adam optimizer<sup>77</sup> with a learning rate of  $10^{-4}$  and a custom loss function  $(1 - DSC)$ , the model employs early

stopping based on validation loss improvement, monitoring metrics like DSC, IoU and binary accuracy.

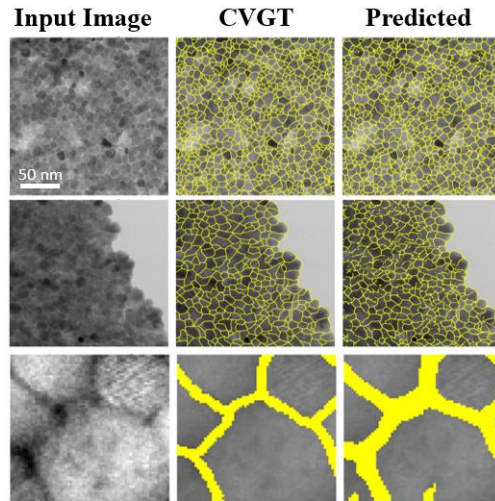
Post-training, the model's performance on test and validation datasets is evaluated, with metrics visualized in Fig. 6d. Analysis reveals that both IoU and DSC metrics in the training and validation sets show rapid initial improvement, then plateau. This indicates the model quickly learns key features of the training data before converging to an optimal solution. Training metrics outperform validation metrics, with training IoU above 0.8 and validation IoU around 0.55, while training DSC nears 1.0 and validation DSC stabilizes at about 0.72. This performance gap is typical in complex segmentation tasks where dropout is not applied<sup>78</sup>, suggesting effective generalization to unseen data without significant overfitting. Given the focus of this work on refining the fragmented segmentation mask, further optimizations like hyperparameter tuning are not pursued. The model's predictions on full-resolution images, critical for analyzing detailed material structures potentially lost or distorted in lower resolutions, demonstrate its efficiency in processing high-resolution images.

The model effectively delineates boundaries in both validation and unseen images, as shown in Figs. 6b and 6c, and in comparisons between CVGTs and predicted masks. It successfully generates segmentation masks for images not included in the training, performing better on images with fewer atomic features and pronounced contrast. Achieving a DSC of 0.72 on the validation dataset, the model aligns with benchmarks in thin segmentation mask tasks, comparable to a DSC of 0.7<sup>70</sup> reported by Jahangard et al. for retinal blood vessel segmentation.

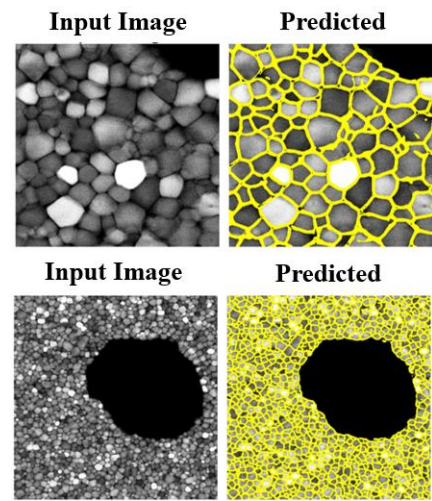
### a. Data Augmentation



### b. Validation Set



### c. Unseen Images



### d. Performance Metrics

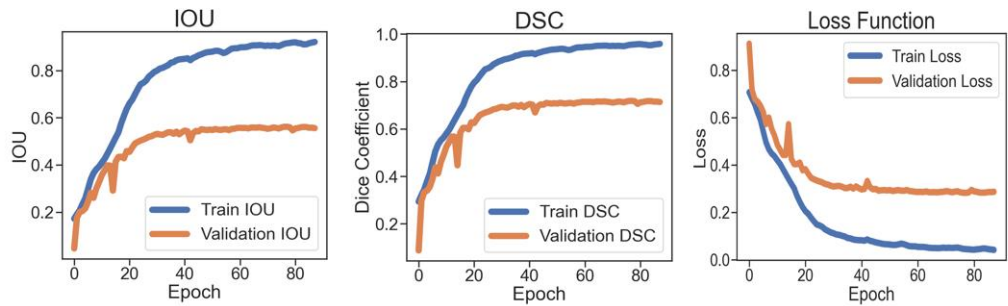


**Fig. 6. Computer vision model training and performance.** **a** One of the original input images and its corresponding data augmentations. **b** Images from the validation set, highlighting the computer vision ground truth (CVGT) and model-predicted fragmented segmentation masks. **c** The model's predictions on unseen images. **d** Plots of the intersection-over-union (IoU) and dice similarity coefficient (DSC) metrics along with the loss function (1-DSC) across training epochs.

### Applying the Hierarchical CRF to Probabilistic Image Labeling

The conditional probability,  $P(Y|X)$ , describes the probability distribution over all possible label configurations  $Y$  given the observed data  $X$ .  $X$  refers to the entire set of observed data over the complete image, containing all of the features (e.g., pixel intensities, color channels, spatial segment information and any other characteristics of the images) that are used to determine the labels  $Y$ .  $Y$  refers to the set of all labels or the complete labeling configuration for an entire image, that is represented as a vector containing the labels for each pixel or segment. On the other hand,  $y$  refers to the label of an individual unit, such as a single pixel or segment. Essentially, each  $y_i$  is an element of the set  $Y = \{y_1, \dots, y_n\}$ .  $Y_{p_i}$  and  $Y_{s_i}$  refer to the label configurations assigned to pixels  $p_i$  and segments  $s_i$  that are part of a set, respectively. The indices  $i$ ,  $j$ , and  $k$  represent the different entities in the image, where  $i$  is the pixel or segment that is currently being labeled, and  $j$  and  $k$  represent other pixels or segments in the same clique as  $i$ . The relationships between  $i$ ,  $j$ , and  $k$  are encapsulated in the pairwise and higher-order terms of the CRF, capturing local and higher-order interactions in the image. The overall probability distribution  $P(Y|X)$  is defined as:

$$P(Y|X) = \frac{1}{Z(X)} \exp\{-E(Y|X)\}, \quad (1)$$

and

$$E(Y|X) = E_u(Y_{s_i}) + E_p(Y_{s_i}, Y_{s_j}) + E_h(Y_{s_i}, Y_{s_j}, Y_{s_k}), \quad (2)$$

where  $E_u(Y_{s_i})$ ,  $E_p(Y_{s_i}, Y_{s_j})$ , and  $E_h(Y_{s_i}, Y_{s_j}, Y_{s_k})$  are the unary, pairwise, and higher-order Gibbs energies, respectively. These energies are calculated based on the labeling of segments  $s_i$ ,  $s_j$ , and  $s_k$ , not just individual pixels.  $Z(X)$  is a partition function that ensures a normalized probability distribution (i.e., between 0 and 1), given by:

$$Z(X) = \sum_{s_i, s_j, s_k} \exp\{-E(Y|X)\}. \quad (3)$$

The unary energy term in Eq. 2,  $E_u(Y_{s_i})$ , is derived from the pixel-based CRF where the unary term is generated by a CNN and the pairwise term is obtained from a Gaussian kernel. Explicitly, for the unary term, the segment-based  $E_u(Y_{s_i})$  can be defined as:

$$E_u(Y_{s_i}) = \Omega^u \mathcal{C} \left( \sum_{p_i \in Y_{s_i}} \Psi_u(y_{p_i}), \sum_{p_i, p_j \in Y_{s_i}, p_i < p_j} \Psi_p(y_{p_i}, y_{p_j}) \right). \quad (4)$$

Here,  $\Omega^u$  represent a global weight and  $\mathcal{C}$  represents a classifier, which identifies pixels as belonging to one of two segment types: complete or broken segments. The set of segments is represented by  $S = S_c \cup S_b = \{s_1, \dots, s_n\}$ , which is the union of two segment sets; complete segments,  $S_c$ , and broken segments,  $S_b$ , respectively. These sets are utilized to create segment cliques, which are groups of interconnected segments categorized into pair cliques, and completion and broken cliques. Sample cliques from each type are shown in Fig. 7a-c, where broken segments are represented in red and completion segments in yellow. The black pixels represent background pixels, gray pixels represent foreground pixels, and white pixels correspond to isolated points. These cliques represent different configurations of segments based on their relationship and interaction with each other. A pair clique,  $C^P$ , shown in Fig. 7a, is comprised of a pair of broken and completion segments. A completion clique,  $C^C$ , shown in Fig. 7b, describes a completion segment and its neighboring broken segments. Finally, a broken clique,  $C^B$ , shown in Fig. 7c, contains all completion segments connecting to either end of a broken segment.

At the classification stage, in addition to the broken and complete segments, triple junctions, isolated points, and the natural curving angles of segments are identified, which are shown in Fig. 7d for a sample section of the segmentation mask. In order to obtain completion segments, first all possible completion segments between all pairs of isolated points are generated, which is shown in Fig. 7e. Then, viable completion segments, which are defined as non-occluding completion segments below a predetermined length, are down selected from all possible segments, which are shown in Fig. 7f. Hence, the classifier maps the unary  $\psi_u(y_{p_i})$  and pairwise  $\psi_p(y_{p_i}, y_{p_j})$  energies of pixels constituting a segment,  $s_i$ , to the segment's unary energy  $E_u(Y_{s_i})$ , where  $\psi_p(y_{p_i}, y_{p_j})$  is given by:

$$\Psi_p(y_{p_i}, y_{p_j}) = \mu(y_{p_i}, y_{p_j}) \sum_{m=1}^K [\omega_p^m k_p^m(f_i, f_j)], \quad (5)$$

where the pairwise-pixel features are given by the following equations:

$$k_p^{(1)}(f_i, f_j) = \omega_p^{(1)} \exp \left\{ - \left[ \frac{|p_i - p_j|^2}{2\theta_a^2} + \frac{|I_i - I_j|^2}{2\theta_b^2} \right] \right\}, \text{ and} \quad (6)$$

$$k_p^{(2)}(f_i, f_j) = \omega_p^{(2)} \exp \left\{ - \left[ \frac{|p_i - p_j|^2}{2\theta_c^2} \right] \right\}.$$

Here,  $\mu(y_{p_i}, y_{p_j})$  is a label compatibility function that follows the Potts model for cost assignments, which states that the cost is non-zero only if the pixels are labeled differently. In other words,  $\mu(y_{p_i}, y_{p_j}) = 1$  if  $(y_{p_i} \neq y_{p_j})$ , and 0 otherwise. For a binary segmentation task, this model punishes similar pixels with different labels. Pairwise terms are calculated using two features involving Gaussian and bilateral filters, which are instrumental in satisfying the similarity

and proximity principles. These principles suggest that pixels that are closely related in intensity and proximity tend to be grouped together.  $\theta_a$ ,  $\theta_b$ , and  $\theta_c$  are the parameters for the Gaussian and bilateral filters that can be adjusted, and  $\omega_p^{(1)}$  and  $\omega_p^{(2)}$  are the corresponding local weights.

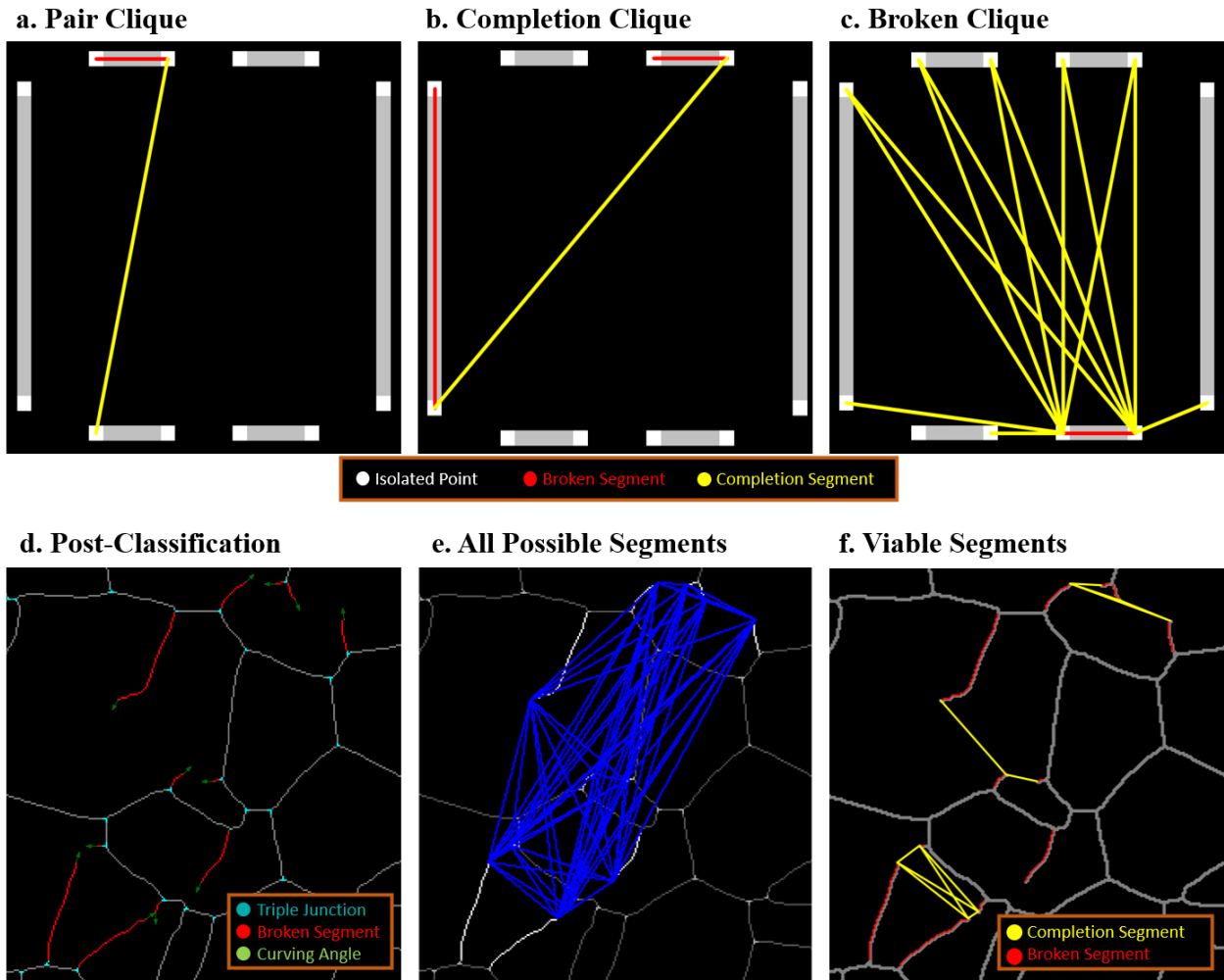


**Fig. 7. Visualization of cliques and classification processes.** **a** Pair Clique ( $\mathcal{C}^P$ ): Interaction between a broken (red) and completion (yellow) segment. **b** Completion Clique ( $\mathcal{C}^C$ ): A completion segment with its neighboring broken segments. **c** Broken Clique ( $\mathcal{C}^B$ ): Completion

segments connecting to a central broken segment. **d** Post-classification detailing broken segments, triple junctions, and natural curving angles in a segmentation mask. **e** All possible completion segments generated between isolated points. **f** Selection of viable completion segments from the generated possibilities.

The significance of closure principle in visual perception, while challenging to encapsulate through local potential functions, is approximated in the study by Ming et al.<sup>53</sup> via a series of localized connectedness constraints. Within a segment's terminal point, two kinds of connectedness constraints are defined, each defined with a series of linear inequalities:

- *The Completion Constraint* is characterized by the limitation that a completion segment can only be activated if its adjacent broken segment is also active, which requires the following inequality to be satisfied:  $y_{s_i} \leq y_{s_j} \quad \forall (s_i \in S_c) \cup (s_j \in S_b) \in C^P$ .
- *The Extension Constraint* is defined by the condition that when a broken segment is active, at least one neighboring completion segment must also be active for possible extension. This is expressed as the inequality:  $y_{s_j} \leq \sum_{s_i} y_{s_i} \quad \forall (s_i \in S_c) \cup (s_j \in S_b) \in C^B$ .

These constraints can be represented in the pairwise term  $E_p(Y_{s_i}, Y_{s_j})$  for segments with the following expression:

$$\begin{aligned}
E_p(Y_{s_i}, Y_{s_j}) = M & \left( \sum_{(s_i \in S_c) \cup (s_j \in S_b) \in C^P} [(1 - y_{s_j}) y_{s_i}] \right. \\
& \left. + \sum_{(s_i \in S_c) \cup (s_j \in S_b) \in C^B} [y_{s_j} \prod (1 - y_{s_i})] \right)
\end{aligned} \tag{7}$$

where  $M$  is a large constant, which is large enough to ensure that Eq. 1 results in a zero-probability configuration (i.e.,  $P(Y|X) = 1/Z(X) \exp\{-M\} \approx 0$ ) in the case that these inequalities are not satisfied.

In line with the law of good figure, which generally favors simpler, more coherent shapes, the higher-order term ( $E_h(Y_{s_i}, Y_{s_j}, Y_{s_k})$ ) is defined to obtain the best possible label configuration that is grounded in the domain expertise. Similar to the models in Ref.<sup>52,53</sup>, different potentials are utilized to define a higher-order Gibbs energy. In this work, the higher-order term is represented as the sum of an interface potential and a complexity potential:

$$\begin{aligned}
E_h(Y_{s_i}, Y_{s_j}, Y_{s_k}) & \\
& = \Omega^I \sum_{(s_i, s_j, s_k) \in C^C} [\Psi_I(y_{s_i}, y_{s_j}, y_{s_k})] \\
& + \Omega^M \sum_{(s_i \in S_c) \cup (s_j, s_k \in S_b)} [\Psi_M(y_{s_i}, y_{s_j}, y_k)],
\end{aligned} \tag{8}$$

where  $\Omega^I$  and  $\Omega^M$  are global weights. The interface potential is defined as:

$$\Psi_I(y_{s_i}, y_{s_j}, y_{s_k}) = \sum_{m=1}^K [\omega_I^m k_I^m(f_i, f_j, f_k)] y_{s_i} y_{s_j} y_{s_k}, \quad (9)$$

where  $\omega_I^m$  are the local weights for  $k_I^m(f_i, f_j, f_k)$ , which represent the interface features. There are seven interface features, the first four of which are obtained from Ref.<sup>53</sup>, and an additional three are considered in this work. The initial four features are: (1) effective corner distance, optimized for capturing sharp turns in contours; (2) effective smooth distance, designed for capturing smoother transitions between segments; (3) angular completion, emphasizes geometric shapes through the sum of angles; and (4) angular difference, useful for identifying parallel or nearly parallel segments. The final three features pertain to the lengths of the two broken segments the one completion segment that forms the clique. Finally, the complexity potential is given by:

$$\Psi_M(y_{s_i}, y_{s_j}, y_{s_k}) = \sum_{m=1}^K [\omega_M^m k_M^m(f_i, f_j, f_k)] y_{s_i} y_{s_j} y_{s_k}, \quad (10)$$

where  $\omega_M^m$  are the local weights for  $k_M^m(f_i, f_j, f_k)$ , which includes two features representing the global complexity. These two features are: (i)  $k_M^{(1)}$ , which is the total effective length of the connected segments, and (ii)  $k_M^{(2)}$ , which represents the angle deviation from the ideal curving angle and the connection angle, effectively controlling the model's overall complexity.

The constraints introduced in Eq. 7 posit that  $y_{s_j}$  and  $y_{s_k}$  can both be active at the same time if and only if  $y_{s_i}$  is also active, therefore simplifying the higher-order term to:

$$\begin{aligned}
& E_h(Y_{s_i}, Y_{s_j}, Y_{s_k}) \\
&= \Omega^I \sum_{(s_i, s_j, s_k) \in C^C} \left[ \sum_{m=1}^K (\omega_I^m k_I^m) \right] y_{s_i} \\
&+ \Omega^M \sum_{(s_i \in S_C) \cup (s_j, s_k \in S_B)} \left[ \sum_{m=1}^K (\omega_M^m k_M^m) \right] y_{s_i}.
\end{aligned} \tag{11}$$

which in turn allows framing the combinatorial optimization problem as a MILP problem, for which the final energy function to be minimized takes the form:

$$\begin{aligned}
& \min \left[ \Omega^u \mathcal{C} \left( \sum_{p_i \in Y_{s_i}} \Psi_u(y_{p_i}), \sum_{p_i, p_j \in Y_{s_i}, p_i < p_j} \mu(y_{p_i}, y_{p_j}) \sum_{m=1}^K [\omega^m k^m(f_i, f_j)] \right) \right. \\
&+ \Omega^I \sum_{(s_i, s_j, s_k) \in C^C} \left[ \sum_{m=1}^K (\omega_I^m k_I^m) \right] y_{s_i} \\
&+ \Omega^M \sum_{(s_i \in S_C) \cup (s_j, s_k \in S_B)} \left[ \sum_{m=1}^K (\omega_M^m k_M^m) \right] y_{s_i},
\end{aligned} \tag{12}$$

subject to  $y_{s_i} \leq y_{s_j} \forall (s_i \in S_C) \cup (s_j \in S_B) \in C^P$  and  $y_{s_j} \leq \sum_{s_i} y_{s_i} \forall (s_i \in S_C) \cup (s_j \in S_B) \in C^B$ . Details pertaining to the implementation of pixel-based and segment-based CRFs are provided in Supplementary Notes 4 and 5, respectively.

## DATA AVAILABILITY

All data generated or analyzed during this study are included in this published article and its supplementary information files.

## **CODE AVAILABILITY**

The underlying code for this study is available in the HierarchicalCRF repository and can be accessed via this link: <https://github.com/dorukaksoy/HierarchicalCRF>.

## **ACKNOWLEDGEMENTS**

This research was primarily supported by the National Science Foundation Materials Research Science and Engineering Center program through the UC Irvine Center for Complex and Active Materials (DMR-2011967). In the preparation of this article, a large language model (ChatGPT September 25, 2023) was employed for tasks such as proofreading, code optimization, and code commentary through careful prompt engineering. While the tool aided in these areas, it was not involved in the conceptualization of the work. All outputs from ChatGPT were rigorously examined for factual accuracy.

## **AUTHOR CONTRIBUTIONS**

**DA:** Formal Analysis; Manual Annotation; Software Development; Methodology; Investigation; Writing - original draft; Writing - review & editing. **HLX:** Writing - review. **TJR:**

Conceptualization; Supervision; Writing - review & editing. **WJB**: Conceptualization; Image Acquisition; Supervision; Funding acquisition; Project Administration; Writing - review & editing.

## **CONFLICT OF INTEREST**

All authors declare no financial or non-financial competing interests.

## 5 REFERENCES

1. Treder, K. P., Huang, C., Kim, J. S. & Kirkland, A. I. Applications of deep learning in electron microscopy. *Microscopy* **71**, i100–i115 (2022).
2. Vahidi, H. *et al.* A Review of Grain Boundary and Heterointerface Characterization in Polycrystalline Oxides by (Scanning) Transmission Electron Microscopy. *Crystals* **11**, 878 (2021).
3. Wardini, J. L., Vahidi, H., Guo, H. & Bowman, W. J. Probing Multiscale Disorder in Pyrochlore and Related Complex Oxides in the Transmission Electron Microscope: A Review. *Front. Chem.* **9**, 743025 (2021).
4. Phillips, P. J., Brandes, M. C., Mills, M. J. & De Graef, M. Diffraction contrast STEM of dislocations: Imaging and simulations. *Ultramicroscopy* **111**, 1483–1487 (2011).
5. Pennycook, S. J. Z-contrast stem for materials science. *Ultramicroscopy* **30**, 58–69 (1989).
6. Wagih, M. & Schuh, C. A. Viewpoint: Can symmetric tilt grain boundaries represent polycrystals? *Scripta Materialia* **237**, 115716 (2023).
7. Yin, W. *et al.* A petascale automated imaging pipeline for mapping neuronal circuits with high-throughput transmission electron microscopy. *Nat Commun* **11**, 4949 (2020).
8. Syed, K. *et al.* Correlations of grain boundary segregation to sintering techniques in a three-phase ceramic. *Materialia* **14**, 100890 (2020).
9. Syed, K., Motley, N. B. & Bowman, W. J. Heterointerface and grain boundary energies, and their influence on microstructure in multiphase ceramics. *Acta Materialia* **227**, 117685 (2022).

10. Najmaei, S. *et al.* Vapour phase growth and grain boundary structure of molybdenum disulphide atomic layers. *Nature Mater* **12**, 754–759 (2013).
11. Aksoy, D. *et al.* Chemical order transitions within extended interfacial segregation zones in NbMoTaW. *J. Appl. Phys.* **132**, 235302 (2022).
12. Patala, S., Mason, J. K. & Schuh, C. A. Improved representations of misorientation information for grain boundary science and engineering. *Progress in Materials Science* **57**, 1383–1425 (2012).
13. Adlakha, I., Tschopp, M. A. & Solanki, K. N. The role of grain boundary structure and crystal orientation on crack growth asymmetry in aluminum. *Materials Science and Engineering A* **618**, 345–354 (2014).
14. Scheiber, D. & Romaner, L. Impact of the segregation energy spectrum on the enthalpy and entropy of segregation. *Acta Materialia* **221**, 117393 (2021).
15. Aksoy, D., Dingreville, R. & Spearot, D. E. An embedded-atom method potential parameterized for sulfur-induced embrittlement of nickel. *Modelling Simul. Mater. Sci. Eng.* **27** 085016, (2019).
16. Aksoy, D., Cao, P., Trelewicz, J. R., Wharry, J. P. & Rupert, T. J. Enhanced radiation damage tolerance of amorphous interphase and grain boundary complexions in Cu-Ta. *arXiv.org* <https://arxiv.org/abs/2309.13474> (2023).
17. Wynblatt, P. & Chatain, D. Anisotropy of segregation at grain boundaries and surfaces. *Metall Mater Trans A* **37**, 2595–2620 (2006).

18. Bowman, W. J., Kelly, M. N., Rohrer, G. S., Hernandez, C. A. & Crozier, P. A. Enhanced ionic conductivity in electroceramics by nanoscale enrichment of grain boundaries with high solute concentration. *Nanoscale* **9**, 17293–17302 (2017).
19. Ko, S.-T. *et al.* Compositionally complex perovskite oxides: Discovering a new class of solid electrolytes with interface-enabled conductivity improvements. *Matter* **6**, 2395–2418 (2023).
20. Bowman, W. J., Yang, J. & Yildiz, B. The role of doping and microstructure on hydrogen solubility in monoclinic ZrO<sub>2</sub>: Experimental validations of simulated defect chemistry. *Acta Materialia* **195**, 172–183 (2020).
21. Bowman, W. J., Darbal, A. & Crozier, P. A. Linking Macroscopic and Nanoscopic Ionic Conductivity: A Semiempirical Framework for Characterizing Grain Boundary Conductivity in Polycrystalline Ceramics. *ACS Appl. Mater. Interfaces* **12**, 507–517 (2020).
22. Bowman, W. J., Zhu, J., Sharma, R. & Crozier, P. A. Electrical conductivity and grain boundary composition of Gd-doped and Gd/Pr co-doped ceria. *Solid State Ionics* **272**, 9–17 (2015).
23. Dingreville, R., Aksoy, D. & Spearot, D. E. A primer on selecting grain boundary sets for comparison of interfacial fracture properties in molecular dynamics simulations. *Sci Rep* **7**, 8332 (2017).
24. Garg, P., Pan, Z., Turlo, V. & Rupert, T. J. Segregation competition and complexion coexistence within a polycrystalline grain boundary network. *Acta Materialia* **218**, 117213 (2021).
25. Aksoy, D., Dingreville, R. & Spearot, D. E. Spectrum of embrittling potencies and relation to properties of symmetric-tilt grain boundaries. *Acta Materialia* **205**, 116527, (2021).

26. Tong, X., Bowman, W. J., Mejia-Giraldo, A., Crozier, P. A. & Mebane, D. S. New Data-Driven Interacting-Defect Model Describing Nanoscopic Grain Boundary Compositions in Ceramics. *J. Phys. Chem. C* **124**, 23619–23625 (2020).
27. Liu, X. *et al.* Monte Carlo simulation of order-disorder transition in refractory high entropy alloys: A data-driven approach. *Computational Materials Science* **187**, 110135 (2021).
28. Long, J., Shelhamer, E. & Darrell, T. Fully convolutional networks for semantic segmentation. in *2015 IEEE Conference on Computer Vision and Pattern Recognition (CVPR)* 3431–3440 (2015).
29. Peregrina-Barreto, H. *et al.* Automatic grain size determination in microstructures using image processing. *Measurement* **46**, 249–258 (2013).
30. Coster, M., Arnould, X., Chermant, J. L., Chermant, L. & Chartier, T. The use of image analysis for sintering investigations: The example of CeO<sub>2</sub> doped with TiO<sub>2</sub>. *Journal of the European Ceramic Society* **25**, 3427–3435 (2005).
31. Gorsevski, P. V., Onasch, C. M., Farver, J. R. & Ye, X. Detecting grain boundaries in deformed rocks using a cellular automata approach. *Computers & Geosciences* **42**, 136–142 (2012).
32. Vimal, M., Sandfeld, S. & Prakash, A. Grain segmentation in atomistic simulations using orientation-based iterative self-organizing data analysis. *Materialia* **21**, 101314 (2022).
33. Salman, N. Image Segmentation Based on Watershed and Edge Detection Techniques. *Int. Arab J. Inf. Technol.* **3**, 104-110 (2006).
34. Roy Choudhury, K., Meere, P. A. & Mulchrone, K. F. Automated grain boundary detection by CASRG. *Journal of Structural Geology* **28**, 363–375 (2006).

35. Liu, A., Lin, W. & Narwaria, M. Image Quality Assessment Based on Gradient Similarity. *IEEE Transactions on Image Processing* **21**, 1500–1512 (2012).
36. Dengiz, O., Smith, A. E. & Nettleship, I. Grain boundary detection in microstructure images using computational intelligence. *Computers in Industry* **56**, 854–866 (2005).
37. Garland, A. P. *et al.* Deep Convolutional Neural Networks as a Rapid Screening Tool for Complex Additively Manufactured Structures. *Additive Manufacturing* **35**, 101217 (2020).
38. Perera, R., Guzzetti, D. & Agrawal, V. Optimized and autonomous machine learning framework for characterizing pores, particles, grains and grain boundaries in microstructural images. *Computational Materials Science* **196**, 110524 (2021).
39. Ragone, M. *et al.* Deep learning for mapping element distribution of high-entropy alloys in scanning transmission electron microscopy images. *Computational Materials Science* **201**, 110905 (2022).
40. Chen, L.-C., Papandreou, G., Schroff, F. & Adam, H. Rethinking Atrous Convolution for Semantic Image Segmentation. *arXiv.org* <https://arxiv.org/abs/1706.05587v3> (2017).
41. He, K., Gkioxari, G., Dollár, P. & Girshick, R. Mask R-CNN. *arXiv.org* <https://arxiv.org/abs/1703.06870v3> (2017).
42. Ronneberger, O., Fischer, P. & Brox, T. U-Net: Convolutional Networks for Biomedical Image Segmentation. *arXiv.org* <https://arxiv.org/abs/1505.04597v1> (2015).
43. Cheng, B., Girshick, R., Dollár, P., Berg, A. C. & Kirillov, A. Boundary IoU: Improving Object-Centric Image Segmentation Evaluation. *arXiv.org* <https://arxiv.org/abs/2103.16562v1> (2021).

44. Li, M., Chen, D., Liu, S. & Liu, F. Grain boundary detection and second phase segmentation based on multi-task learning and generative adversarial network. *Measurement* **162**, 107857 (2020).
45. Li, S. F., Mason, J. K., Lind, J. & Kumar, M. Quadruple nodes and grain boundary connectivity in three dimensions. *Acta Materialia* **64**, 220–230 (2014).
46. Burke, J. E. & Turnbull, D. Recrystallization and grain growth. *Progress in Metal Physics* **3**, 220–292 (1952).
47. Papari, G. & Petkov, N. Edge and line oriented contour detection: State of the art. *Image and Vision Computing* **29**, 79–103 (2011).
48. Sutton, C. An Introduction to Conditional Random Fields. *FNT in Machine Learning* **4**, 267–373 (2012).
49. Arnab, A. *et al.* Conditional Random Fields Meet Deep Neural Networks for Semantic Segmentation: Combining Probabilistic Graphical Models with Deep Learning for Structured Prediction. *IEEE Signal Process. Mag.* **35**, 37–52 (2018).
50. Shotton, J., Winn, J., Rother, C. & Criminisi, A. TextonBoost for Image Understanding: Multi-Class Object Recognition and Segmentation by Jointly Modeling Texture, Layout, and Context. *Int J Comput Vis* **81**, 2–23 (2009).
51. Krähenbühl, P. & Koltun, V. Efficient Inference in Fully Connected CRFs with Gaussian Edge Potentials. *arXiv.org* <http://arxiv.org/abs/1210.5644> (2012).
52. Delong, A., Osokin, A., Isack, H. N. & Boykov, Y. Fast approximate energy minimization with label costs. in *2010 IEEE Computer Society Conference on Computer Vision and Pattern Recognition* 2173–2180 (IEEE, 2010). doi:10.1109/CVPR.2010.5539897.

53. Yansheng Ming, Hongdong Li, & Xuming He. Connected contours: A new contour completion model that respects the closure effect. in *2012 IEEE Conference on Computer Vision and Pattern Recognition* 829–836 (IEEE, 2012). doi:10.1109/CVPR.2012.6247755.
54. Woeginger, G. J. Exact Algorithms for NP-Hard Problems: A Survey. in *Combinatorial Optimization — Eureka, You Shrink!: Papers Dedicated to Jack Edmonds 5th International Workshop Aussois, France, March 5–9, 2001 Revised Papers* (eds. Jünger, M., Reinelt, G. & Rinaldi, G.) 185–207 (Springer, 2003). doi:10.1007/3-540-36478-1\_17.
55. Price, K. V. Differential Evolution. in *Handbook of Optimization: From Classical to Modern Approach* (eds. Zelinka, I., Snáśel, V. & Abraham, A.) 187–214 (Springer, 2013). doi:10.1007/978-3-642-30504-7\_8.
56. Williams, L. R. & Jacobs, D. W. Stochastic completion fields: A neural model of illusory contour shape and salience. *Neural Computation* **9**, 837–858 (1997).
57. Rezanejad, M. *et al.* Contour-guided Image Completion with Perceptual Grouping. Preprint at <https://doi.org/10.48550/arXiv.2111.11322> (2021).
58. Howden, W. E. The sofa problem. *The Computer Journal* **11**, 299–301 (1968).
59. Simonyan, K. & Zisserman, A. Very Deep Convolutional Networks for Large-Scale Image Recognition. Preprint at <https://doi.org/10.48550/arXiv.1409.1556> (2015).
60. Minaee, S. *et al.* Image Segmentation Using Deep Learning: A Survey. Preprint at <https://doi.org/10.48550/arXiv.2001.05566> (2020).
61. Caselles, V., Kimmel, R. & Sapiro, G. Geodesic Active Contours. *International Journal of Computer Vision* **22**, 61–79 (1997).

62. Zheng, S. *et al.* Conditional Random Fields as Recurrent Neural Networks. in *2015 IEEE International Conference on Computer Vision (ICCV)* 1529–1537 (IEEE, 2015). doi:10.1109/ICCV.2015.179.
63. Mullins, W. W. Two-Dimensional Motion of Idealized Grain Boundaries. *Journal of Applied Physics* **27**, 900–904 (2004).
64. Seita, M. *et al.* A high-throughput technique for determining grain boundary character non-destructively in microstructures with through-thickness grains. *npj Comput Mater* **2**, 1–5 (2016).
65. Martin, D. R., Fowlkes, C. C. & Malik, J. Learning to detect natural image boundaries using local brightness, color, and texture cues. *IEEE Trans. Pattern Anal. Machine Intell.* **26**, 530–549 (2004).
66. Cheuk Yiu Ip, Varshney, A. & JaJa, J. Hierarchical Exploration of Volumes Using Multilevel Segmentation of the Intensity-Gradient Histograms. *IEEE Trans. Visual. Comput. Graphics* **18**, 2355–2363 (2012).
67. Gauch, J. M. Image segmentation and analysis via multiscale gradient watershed hierarchies. *IEEE Transactions on Image Processing* **8**, 69–79 (1999).
68. Cantwell, P. R. *et al.* Grain Boundary Complexion Transitions. *Annual Review of Materials Research* **50**, 465–492 (2020).
69. Kunselman, C., Sheikh, S., Mikkelsen, M., Attari, V. & Arróyave, R. Microstructure classification in the unsupervised context. *Acta Materialia* **223**, 117434 (2022).
70. Jahangard, S., Zangooei, M. H. & Shahedi, M. U-Net Based Architecture for an Improved Multiresolution Segmentation in Medical Images. (2020) doi:10.48550/ARXIV.2007.08238.

71. Ikeno, H., Kumaraswamy, A., Kai, K., Wachtler, T. & Ai, H. A Segmentation Scheme for Complex Neuronal Arbors and Application to Vibration Sensitive Neurons in the Honeybee Brain. *Frontiers in Neuroinformatics* **12**, (2018).
72. Chen, C. *et al.* Deep Learning for Cardiac Image Segmentation: A Review. *Frontiers in Cardiovascular Medicine* **7**, (2020).
73. Keles, E., Irmakci, I. & Bagci, U. Musculoskeletal MR Image Segmentation with Artificial Intelligence. *Advances in Clinical Radiology* **4**, 179–188 (2022).
74. Lai, P.-Y., Chang, C.-H., Su, H.-R. & Kuo, W.-C. Lymphatic vessel segmentation in optical coherence tomography by adding U-Net-based CNN for artifact minimization. *Biomed. Opt. Express, BOE* **11**, 2679–2693 (2020).
75. Zhang, M. *et al.* A neural network approach to segment brain blood vessels in digital subtraction angiography. *Computer Methods and Programs in Biomedicine* **185**, 105159 (2020).
76. He, K., Zhang, X., Ren, S. & Sun, J. Deep Residual Learning for Image Recognition. Preprint at <https://doi.org/10.48550/arXiv.1512.03385> (2015).
77. Kingma, D. P. & Ba, J. Adam: A Method for Stochastic Optimization. Preprint at <https://doi.org/10.48550/arXiv.1412.6980> (2017).
78. Zhao, R. *et al.* Rethinking Dice Loss for Medical Image Segmentation. in *2020 IEEE International Conference on Data Mining (ICDM)* 851–860 (2020). doi:10.1109/ICDM50108.2020.00094.

# Human Perception-Inspired Grain Segmentation Refinement Using Conditional Random Fields

Doruk Aksoy<sup>1, \*</sup>, Huolin L. Xin<sup>2</sup>, Timothy J. Rupert<sup>1, 3</sup>, William J. Bowman<sup>1, \*</sup>

<sup>1</sup> Department of Materials Science and Engineering, University of California, Irvine, CA 92697, USA

<sup>2</sup> Department of Physics and Astronomy, University of California, Irvine, CA 92697, USA

<sup>3</sup> Department of Mechanical and Aerospace Engineering, University of California, Irvine, CA 92697, USA

\* Corresponding authors: [daksoy@uci.edu](mailto:daksoy@uci.edu), [will.bowman@uci.edu](mailto:will.bowman@uci.edu)

## Supplementary Information

### Supplementary Note 1: Pathfinding

The pathfinding algorithm is designed to trace the path between a source and a sink within each field in the least costly way. For this task, first a base pattern is generated. The base pattern, shown in Fig. S1(a), acts as a cost map where the central pixel is assigned a low cost, which increases radially away from the center. The rate of cost increase is determined from an exact 2D Gaussian distribution. This distribution is subsequently down sampled to a specific size while preserving its characteristic shape. A right-handed orientation is utilized when defining the curving angles, with angles calculated with respect to the positive x axis. To encourage path tracing in this direction, the costs of the right-hand side of the pattern are decreased by a quarter of the original costs, as illustrated in Fig. S1 (b). The algorithm involves several hyperparameters, including the standard deviation of the Gaussian distribution, and the lowest and highest costs, which aid in fine-tuning the shape and costs associated with the base pattern. This base pattern is then applied around each isolated point linked with a particular completion segment, represented by an isolated point pair in Fig. S1(c). Finally, the base pattern is oriented according to the natural curving angle of the isolated point, as can be observed in Fig. S1(d), where orientations for both source and sink points are delineated.

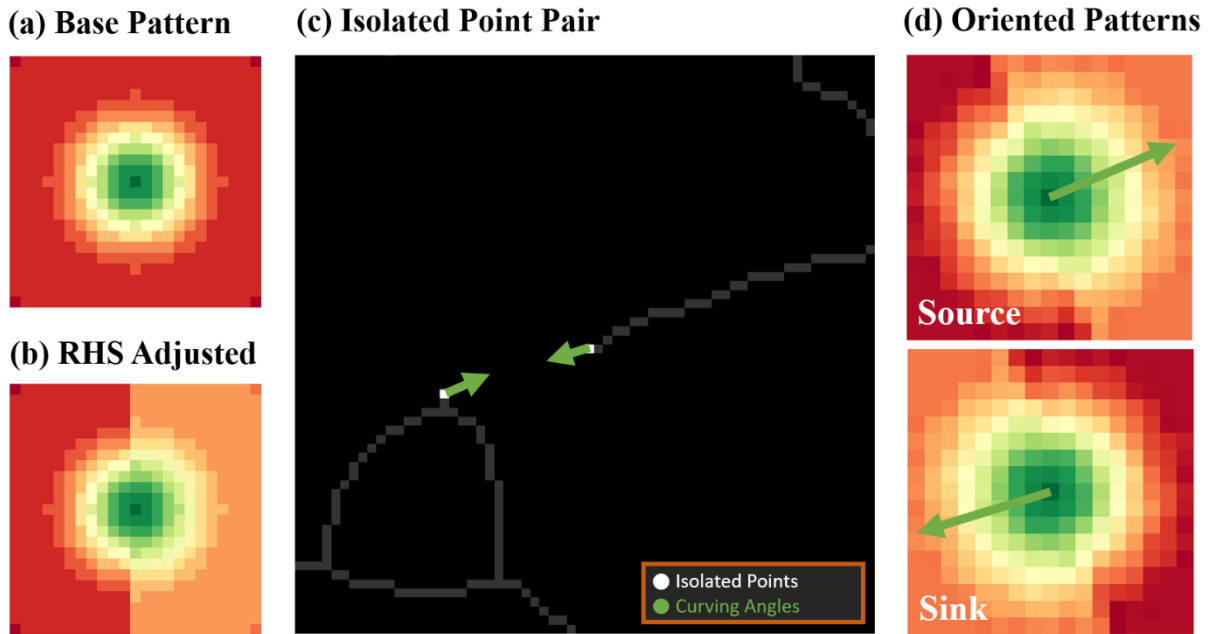


**Fig. S1. Illustration of the pathfinding algorithm's base patterns.** (a) The base pattern generated as a cost map based on a 2D Gaussian distribution, where costs increase radially from the center. (b) The adjusted right-hand side of the base pattern, with costs decreased to favor path tracing in that direction. (c) Depicts an isolated point pair used in the completion segment. (d) Exhibits the orientation of the base pattern according to the natural curving angles for both source (top) and sink (bottom) points.

The oriented base patterns are then placed on both source and sink points, ensuring alignment with the direction of the desired path. In the field, all remaining pixels are assigned the highest cost of the base pattern, except for the foreground (non-traversable) pixels, which are assigned very high costs to ensure a non-occluding path. In the resulting cost map, the immediate local environment of the source and sink points in the direction of their respective curving angles are the lowest cost pixels, where the cost increases as divergence from the original angle occurs and as the distance from the source or sinks increases. The cost map is carefully constructed to handle out-of-bounds exceptions, ensuring that the sink is never at the very edge of the field.

For the heuristics of the A\* algorithm, the Chebyshev distance is calculated by measuring the greater of the horizontal or vertical distances between the source and the sink. This distance measure is selected to ensure that the 8 neighbors of the central pixel have the same

costs, so as not to interfere with the previously generated base pattern. A weighted grid, corresponding to the field, is created, with walls representing non-traversable pixels and weights assigned according to the previously generated cost map, which is then used to obtain the lowest-cost shortest path based on the heuristics.

### **Supplementary Note 2: Watershed Segmentation**

For the application of the marker-based watershed segmentation in this work, the image is inverted, transforming the background to a value of 1 and the foreground to 0. To eliminate isolated background pixels, a dilation operation is applied to the inverted image. Subsequently, the Euclidean distance from every binary pixel to the nearest zero pixel is computed. Peaks in this distance map, which correspond to local maxima, are identified. These peaks are then used to create a mask, marking each with a unique identifier to serve as markers for the watershed operation.

The watershed algorithm is applied to the negative of the distance map, using the previously identified markers. This operation aims to fill regions enclosed by edges, effectively segmenting the image. Following the watershed operation, the regions are dilated to further refine the segmentation. Single-pixel regions, which can be considered as noise or artifacts, are addressed using a grey erosion operation. This operation replaced each pixel with the minimum value of its neighbors, effectively spreading labels from larger regions into these single-pixel regions.

### **Supplementary Note 3: Performance Evaluation Metrics**

In assessing the model's performance, a multi-metric approach is employed to capture various aspects of the algorithm's efficacy and reliability. To calculate these metrics, first true positives (tp), true negatives (tn), false positives (fp), and false negatives (fn) are obtained. These elements form the confusion matrix, which is essential for calculating diverse performance metrics and offers a detailed assessment of the model's classification capabilities.

Pixel accuracy is computed as the ratio of the accurately classified pixels to the total number of pixels, formulated as  $Accuracy = (tp + tn)/(tp + fp + tn + fn)$ . While

straightforward, pixel accuracy may not be adequate for imbalanced datasets, as it can provide a misleadingly optimistic view.

IoU, also known as Jaccard's Index, is calculated using the formula  $IoU = \frac{|X \cap Y|}{|X| + |Y|} = \frac{tp}{tp + fp + fn}$ . Here,  $|X \cap Y|$  and  $|X| + |Y|$  represent the overlap and union between the true and predicted label sets, respectively. The DSC is similarly employed and is given by  $DSC = \frac{2|X \cap Y|}{|X| + |Y|} = \frac{2tp}{2tp + fp + fn}$ . Both IoU and DSC provide valuable insights into the quality of the object-level segmentation by emphasizing the correctly classified overlapping areas.

Precision and recall are defined as  $Precision = tp/(tp + fp)$  and  $Recall = tp/(tp + fn)$ , respectively. Precision evaluates the model's ability to avoid false positives, while recall assesses the identification of all relevant instances. The ROC curve plots the true positive rate (recall)  $(tp/(tp + fn))$  against the false positive rate  $(fp/(fp + tn))$  at various classification thresholds. The area under the ROC curve is often calculated as a summary metric, with an area equal to 1 corresponding to the perfect classification, and the diagonal line corresponding to a random guess. Similarly, the precision-recall curve is used to depict the trade-off between precision and recall at different thresholds, where a high area under the curve indicating both high recall and high precision.

#### **Supplementary Note 4: Pixel-based CRF**

To address the segmentation refinement, pixel-based CRFs are applied, ensuring the laws of proximity and similarity are satisfied. For this task, a linear fully connected CRF is utilized, with its predictions obtained by an approximate inference algorithm<sup>1</sup>. The energetic contributions of pixel pairs are defined by a linear combination of Gaussian and bilateral pairwise potentials. The bilateral potential contributes to both proximity and similarity laws, as it considers the proximity of two pixels and intensity similarity (matching colors are grouped together), while the Gaussian potential is associated with the proximity law by removing the isolated point groups.

The input image and fragmented segmentation mask are transformed and normalized to be compatible with the CRF model. The CRF model is initialized with two classes, unary energy is

set, and pairwise Gaussian and bilateral potentials are added, with symmetric normalization. Inference is performed for five iterations to obtain the refined binary segmentation mask, which subsequently undergoes a skeletonization process to enhance segmentation precision. Skeletonization is a technique used to eliminate extraneous pixels and reduce a segmented object to its essential structure, represented as a single pixel-wide mask that preserves the object's general shape and connectivity<sup>2</sup>. The Cython-based Python wrapper repository PyDenseCRF is utilized for this task<sup>3</sup>.

The next step involves identifying and classifying various image elements, such as triple junctions, complete and broken segments, and isolated points. Triple junctions are identified as the foreground (interface) pixels where at least three immediate or five second-nearest neighbors are also foreground pixels, which is achieved through a convolution-based approach, examining the neighbors of each pixel in a binary image array.

Following the identification of triple junctions, segments are classified. Segments are defined as collections of connected foreground pixels located between triple junctions. The application of a convolution kernel aids in counting the immediate neighbors for each pixel, thereby facilitating the differentiation of segments and isolated points. Isolated points are indicative of broken segments and are characterized by pixels having only one neighbor.

The segments are then categorized as either broken or complete, with broken segments containing at least one isolated point, and complete segments not containing any. Each segment is assigned a unique label, resulting in distinct arrays for broken and complete segments. The natural curvature of broken segments is determined by calculating angles, initially between the isolated point and its neighboring pixel, and subsequently through a more sophisticated sliding window approach. This approach considers the entire broken segment, computing an average angle across sliding windows for a more accurate representation of curving angles.

### **Supplementary Note 5: Segment-based CRF**

To construct all possible paths within a given distance, a graph is formed where nodes represented isolated points and edges represented potential paths between them. To be assigned as an edge, the length of the path should be less than a predetermined pixel distance

value (64 pixels is selected in this work), and should not occlude with any foreground pixels. Then, the edges of this graphs are assigned as completion segments. These segments, along with broken segments, formed the basis for identifying cliques and computing image features.

Cliques, in this context, are groups of image segments that are closely related or connected. They are formed in three categories: pair, completion, and broken. Pair cliques are identified by checking if any completion segment touched a broken segment. Completion cliques are formed by associating the two broken segments with each completion segment. Broken cliques are identified by finding all segments connecting to either endpoint of a broken segment. The formation of these cliques is required for the computation of interface features and the subsequent optimization process.

Once the cliques are formed, interface features are computed for each type of clique, to understand the spatial and geometric relationships between different segments. The final three features are the lengths of the two broken and one completion segments forming the clique obtained by the Euclidean distances between the start and endpoints of each segment. To calculate the first four features, for each completion segment, lines are extended from the isolated points in the direction of the curving angles, and the intersection of these lines is determined. If an intersection is identified, the effective corner distance is determined through the Euclidean distance between points forming the edges connected to the intersection. The effective smooth distance is calculated using the centroid of the triangle formed by the intersection and the endpoints of the completion segment, with the arc length representing the smooth distance in cases where a radius is defined. A sample image illustrating the interface features is shown in Fig. 1 (d) in the main article. If no radius is defined, the effective corner distance is selected as the smooth distance. The angles between the completion segment and the edges connected to the intersection are also calculated and incorporated into the feature vector.

Conversely, if no intersection is detected, the y and x coordinate differences between the endpoints of the completion segment are employed to calculate the effective corner and smooth distances. In scenarios where both differences are non-zero, the smooth distance is calculated similarly to when an intersection is present. If either difference is zero, the Euclidean distance between the endpoints served as both the effective corner and smooth distances. The

angles between the lines are subsequently calculated and included in the feature vector. Two parameters, alpha and beta, are used to weigh the contribution of these angular features, ensuring a balanced representation of the geometric relationships. These computations provided insights into the spatial arrangement and curvature of the segments.

The first complexity potential feature is determined based on the effective length of each completion segment and neighboring broken segments, calculated using the Euclidean distance between the start and end points. This feature represented the spatial extent of the completion segments, contributing to the overall understanding of the image's geometric structure. The second feature, which is based on the angle deviation between the two neighboring broken segments of a completion segment, is calculated using the ideal angles derived from the relative positions of the two points forming the segments. Deviation is assessed by comparing the actual curving angles of these points to the ideal angles. The total deviation is obtained by summing up the deviations of the two points. This angle deviation metric captures the geometric compatibility between the two neighboring broken segments and the completion segment, thus providing insight into the image's overall geometric coherence and continuity.

The optimal solution to the CRF is the label configuration for each broken and completion segment that minimizes the objective function. The objective function is defined as the difference between the label configuration predicted by the model and the FSGT, serving as a measure of how well the model performed in predicting potential paths compared to a human. This function is subjected to extension and completion constraints. Subsequently, fields around the completion segments to be connected are extracted. A field is a subset of the image centered around an isolated point, and it is used to analyze the local environment of that point. The extraction of fields around these paths are crucial for analyzing the local characteristics of the segmentation and ensuring the continuity and connectivity of the segments. During the extraction, one of the isolated points on a completion segment is designated as the source, and the other one is assigned as the sink. The field around the source is extracted, and the relative coordinates of the sink within the field are determined. This process results in a collection of fields, each with a designated source and sink, representing the local environment of isolated points in the completion segments, which are then utilized by the pathfinding algorithm<sup>4</sup>.

## Supplementary References

1. Krähenbühl, P. & Koltun, V. Efficient Inference in Fully Connected CRFs with Gaussian Edge Potentials. Preprint at <http://arxiv.org/abs/1210.5644> (2012).
2. Zhang, T. Y. & Suen, C. Y. A fast parallel algorithm for thinning digital patterns. *Commun. ACM* **27**, 236–239 (1984).
3. PyDenseCRF, <https://github.com/lucasb-eyer/pydensecrf>.
4. Red Blob Games. A\* algorithm implementation, <https://www.redblobgames.com/pathfinding/a-star/implementation.html>.